

Thermal Conductivity of Cryogenic Deuterium

Alan She

Pittsford Mendon High School
Pittsford, NY

Advisor: Dr. R. S. Craxton

Laboratory for Laser Energetics
University of Rochester
Rochester, NY

November 2007

Abstract

Accurate values of the thermal conductivity and specific heat of deuterium are necessary to make high quality cryogenic laser fusion targets. Due to the difficulty of measuring these values at cryogenic temperatures, the “3 ω ” method is used. This involves passing an oscillating current through a platinum wire embedded in deuterium and measuring the third-harmonic voltage that results from the temperature dependence of the resistance. A two dimensional model has been built that calculates heat flow in both the axial and radial directions (i.e., along and perpendicular to the wire) including the frequency-dependent skin depth. The model has been fit to four sets of experimental data (the wire in a vacuum and in gaseous, liquid, and solid deuterium) by adjusting the parameters of thermal conductivity and specific heat. Generally, the model and data agree well. The model has enabled the thermal conductivity to be accurately determined at cryogenic temperatures for gaseous, liquid, and solid deuterium.

1. Introduction

The thermal conductivity of deuterium is used in the modeling of cryogenic laser fusion targets. In this process, a small fuel pellet, consisting of a mixture of deuterium and tritium, is heated and compressed by high-energy laser beams. This creates conditions similar to those of the Sun, allowing the nuclear fusion of deuterium and tritium to occur through the reaction



Energy is released in the form of the kinetic energy of the resulting neutron. The fuel pellet is initially kept at cryogenic temperatures to maximize the amount of fuel in the small volume.

Knowledge of the thermal conductivity of deuterium is necessary for modeling the heat flow within the target.¹ Knowing the conductivity to better precision improves target quality. The conductivity is also used in modeling the behavior of the target when exposed to the environment.

Initially, the target is covered by a “shroud” to protect it from the environment. Immediately before the laser shot, the shroud is quickly removed. It is of interest to model what happens in the interval between the removal of the shroud and the shot, such as the rate of increase of pressure in the center of the target due to the conduction of heat resulting from external radiation.

In 1954, early measurements of the thermal conductivity of deuterium were made by Powers.² The setup was of the parallel plate type, where heat was deposited at a known rate at one end of a cylinder containing deuterium and exited through a heat bath at the other end. The temperature gradient across the cylinder was measured by a multiple-junction-difference thermocouple. The experiment was prone to errors including heat flow into the walls (requiring correction), convection due to the geometry of the setup, and lack of symmetry from the intrusion of measurement devices.

First introduced by Cahill³ in 1986 and subsequently used by various authors,^{4,8} the 3ω method measures thermal conductivity in a geometry where the avenues of heat flow are simpler to accommodate than in previous methods. There is also less susceptibility to convection. The method uses a wire or thin film as both a heater and a thermometer to produce and measure temperature oscillations in a chosen medium.

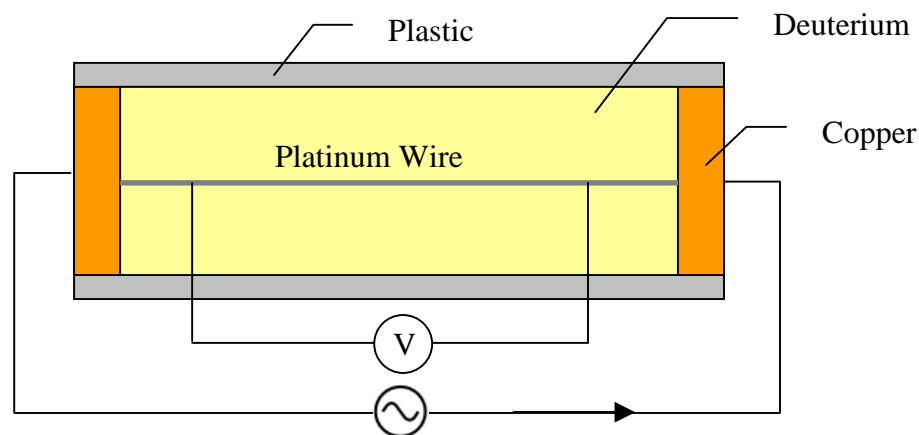


Figure 1.1 Diagram of the experiment. An oscillating current is passed through the wire, and the voltage across a portion of the wire is measured. The plastic and copper are heat baths.

In recent experiments,⁹ the 3ω method was used to determine the thermal conductivity of cryogenic deuterium. As indicated in Figure 1.1, a platinum wire is embedded in deuterium. A sinusoidal current through the wire deposits heat into the system. Heat exits the system by the heat baths, which are set at the desired temperature. The time-averaged thermal equilibrium of the system (“steady state”) is established after a brief interval, after which the voltage across a portion of the wire is measured. The temperature dependence of the resistance of the wire results in a small third-harmonic voltage, which has both in-phase and out-of-phase components with respect to the phase of the power. It is possible to determine the oscillatory temperature from this voltage. The temperature is out of phase with the oscillating power at high drive frequencies and in phase in the limit as the frequency approaches zero.

A computer program was built to model this experiment. The model accounts for the two-dimensional (2D) geometry of the experiment (there is thermal conduction parallel and perpendicular to the wire). It has been used to determine the significance of the 2D effects and to provide improved accuracy over the one-dimensional (1D) numerical solutions, which ignore heat flow along the wire, that were previously used to model experiments.¹⁰ By matching the predicted temperature amplitudes of the program to the experimental data, the thermal conductivities of solid, liquid, and gaseous deuterium have been determined.

2. Analysis of the 3ω Method

This section shows how the amplitude of the temperature oscillations in the wire can be determined from the experimentally obtained voltages.

The resistance of the wire changes with the temperature T :

$$R = R_0 + \alpha(T - T_0), \quad (2-1)$$

where R_0 is the resistance at temperature T_0 and α is a constant ($\alpha = dR/dT$).

The sinusoidal current applied to the wire can be expressed in complex form:

$$I(t) = I_{0s} \sin(\omega t) + I_{0c} \cos(\omega t) = \frac{1}{2} [\tilde{I} e^{i\omega t} + \tilde{I}^* e^{-i\omega t}], \quad (2-2)$$

where \tilde{I} is complex and \tilde{I}^* indicates its complex conjugate. Generally, $I_{0s} = 0$ and \tilde{I} is real. The temperature has a steady time-averaged component, $T_1(t)$, and real and imaginary components that are in phase and out of phase with the power, respectively:

$$T(t) = T_1(t) + \frac{1}{2} [\tilde{T} e^{2i\omega t} + \tilde{T}^* e^{-2i\omega t}]. \quad (2-3)$$

The temperature oscillates at the second harmonic, since the power, $P = I^2 R$, brings in $e^{2i\omega t}$ terms from (2-2). Using (2-1) to (2-3), the voltage across the wire is

$$V(t) = I(t)R(t) = \frac{1}{2} [\tilde{I} e^{i\omega t} + \tilde{I}^* e^{-i\omega t}] \left\{ R_0 + \alpha \left[T_1(t) + \frac{1}{2} [\tilde{T} e^{2i\omega t} + \tilde{T}^* e^{-2i\omega t}] - T_0 \right] \right\}, \quad (2-4)$$

which can be written as

$$V(t) = \frac{1}{2} [\tilde{V}_\omega e^{i\omega t} + \tilde{V}_\omega^* e^{-i\omega t} + \tilde{V}_{3\omega} e^{3i\omega t} + \tilde{V}_{3\omega}^* e^{-3i\omega t}], \quad (2-5)$$

where

$$\tilde{V}_\omega \approx \tilde{I} R_0 \quad \text{and} \quad \tilde{V}_{3\omega} = \frac{1}{2} \alpha \tilde{T} \tilde{I}. \quad (2-6)$$

The amplitude of the first harmonic voltage is the product of the current and the time-averaged resistance, and the amplitude of the third harmonic voltage is proportional to the product of the first harmonic current and the second harmonic temperature.

Dividing the two parts of (2-6) to eliminate the current shows that the amplitude of the temperature oscillation can be determined from the ratio of the third harmonic voltage to the first harmonic voltage:^{10,11}

$$\tilde{T} = 2 \frac{\tilde{V}_{3\omega} R_0}{\tilde{V}_\omega \alpha}. \quad (2-7)$$

3. 2D Computer Model

A 2D computer model was built to model the experiment. It was constructed in (R, Z) geometry: perpendicular and parallel to the wire, respectively (see Figure 2.1). The model includes the platinum wire, deuterium, and the surrounding heat baths.

The radius of the wire (7.5 μm) is small when compared to the radial width of the deuterium medium (1 to 3 mm), and hence a variable-size grid was implemented in the deuterium, wherein the radial widths of the cells increase geometrically with their distance from the wire. The cell widths in Z are kept uniform for all media. The average of the platinum and deuterium conductivities is used as the conductivity at the platinum-deuterium boundary. There is no heat flux across the lower boundary of the platinum wire (the Z axis).

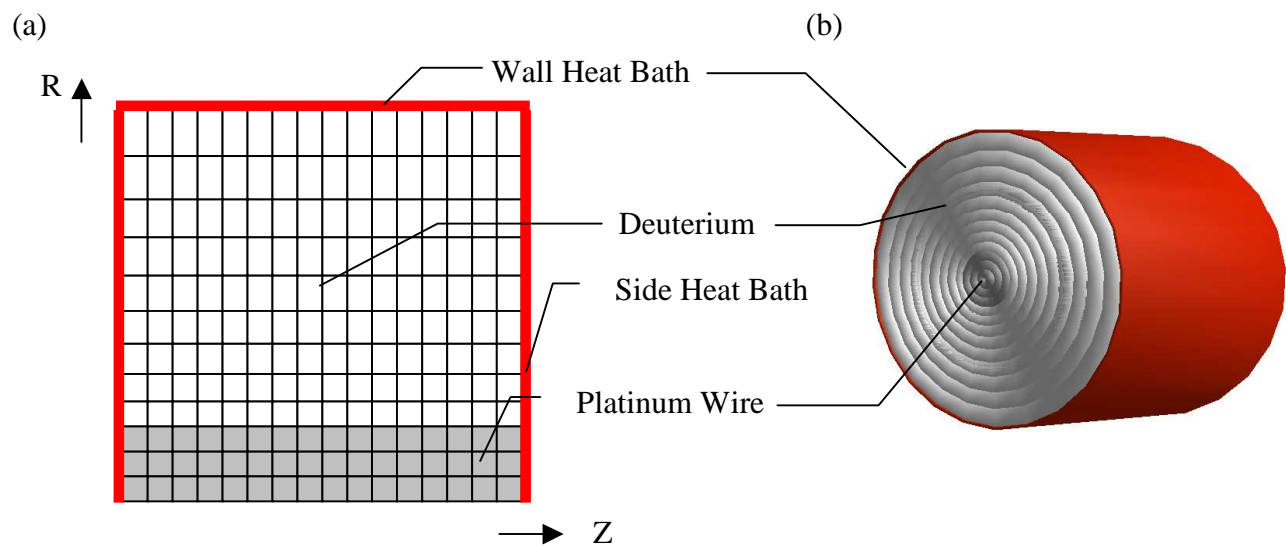


Figure 2.1 (a) A depiction of the computer model including the cells used to solve the heat flow equation. Side heat baths and the wall heat bath are named differently for identification but function identically. (b) A 3D depiction of the model, where each cell is a ring.

The equation solved for each cell is

$$C \frac{\partial T}{\partial t} + \nabla \cdot Q = W, \quad (3-1)$$

where the heat flux Q is given by

$$Q = -\kappa \nabla T. \quad (3-2)$$

Here C is the specific heat of the cell, T is the temperature, κ is the thermal conductivity and W is the heat deposited per unit volume. This can be solved as an initial value problem to give the full solution of the form (2-3), or it can be solved for the complex \tilde{T} in the “steady state,” in which case $\partial T / \partial t$ is replaced with $\frac{1}{2}(2i\omega)[\tilde{T}e^{2i\omega t} - \tilde{T}^*e^{-2i\omega t}]$.

The initial value solution is given by

$$C \frac{T' - T}{\Delta t} - [\theta \nabla \cdot \kappa \nabla T' + (1 - \theta) \nabla \cdot \kappa \nabla T] = W, \tag{3-3}$$

where Δt is the time step, T' is the temperature after the time step, and θ is a numerical parameter between 0 and 1. When $\theta = 0$, T' at each cell is given explicitly in terms of known quantities. However, the small Δt necessary for stability¹² requires many time steps to reach the “steady state”. For $\theta \geq 0.5$, stability is achieved however large Δt is.¹² The choice $\theta = 1$ is typically made. This gives a backward difference equation in which the $\nabla T'$ terms couple the unknown T' at each cell center to the T' at the four adjacent cells.

Whether the initial value solution (T') with $\theta > 0$ or the “steady state” solution (\tilde{T}) is required, a set of simultaneous equations result that can be solved via matrix inversion (see Appendix). The program constructs a quindagonal coefficient matrix that corresponds to a grid of cells as illustrated in the simplified grid of Figure 3.1.

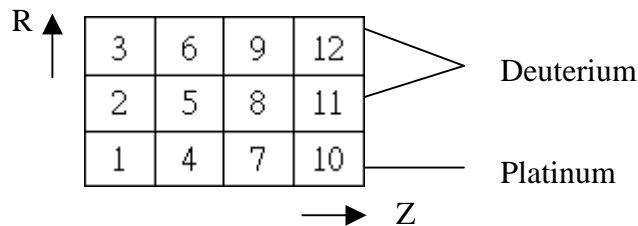


Figure 3.1 A simplified 3x4 grid.

For this grid, with the bottom row as the platinum wire and the top two rows as the deuterium, there is a corresponding 12x12 quindagonal matrix equation:

Figure 4.1 shows the temperature at the center of the wire as a function of time. It takes about 30 ms to reach the “steady state”, which is when the measurements are taken in the experiment. Also, it can be seen that the temperature oscillations are out of phase with the power.

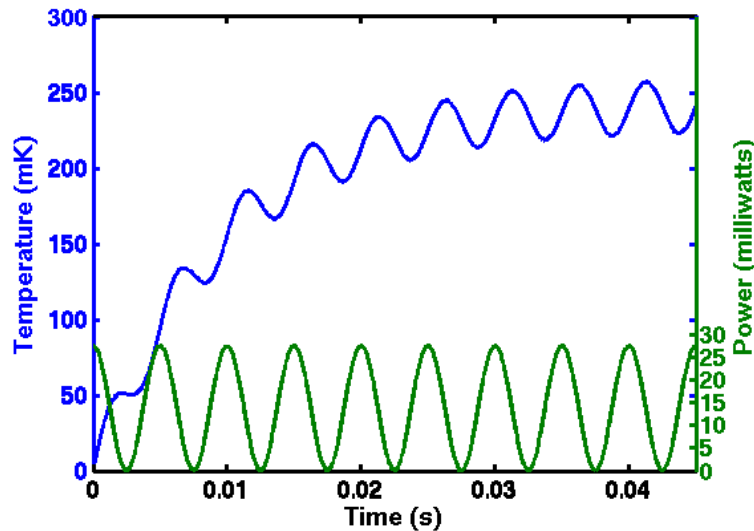


Figure 4.1 Graphs of the temperature in the center of the wire and the power against time for a platinum wire in vacuum with the current oscillating at 100 Hz.

The spatial dependence of the 1D steady-state solutions along Z is shown in Figure 4.2 for four frequencies from 1 Hz to 1000 Hz. The temperature amplitude is zero at each end due to the side heat baths. At different frequencies the temperature amplitudes along Z have distinctive shapes, which can be understood in terms of the “penetration depth”¹⁰ (d) of the temperature amplitudes. The penetration depth is a measure of how far the temperature oscillations penetrate before falloff and is a function of frequency, thermal conductivity, and specific heat:²

$$d = \sqrt{\frac{\kappa}{2\omega \cdot C}}. \quad (4-1)$$

The penetration depth shortens as the frequency increases because there is insufficient time for the changes in temperature to be thoroughly transmitted.

At low frequencies of 10 Hz and less, the temperature profiles (Figures 4.2a and 4.2b) maintain the arch shape, showing the relatively complete penetration of the temperature changes. The quadratic shape results from the maximum temperature being at the middle of the wire.

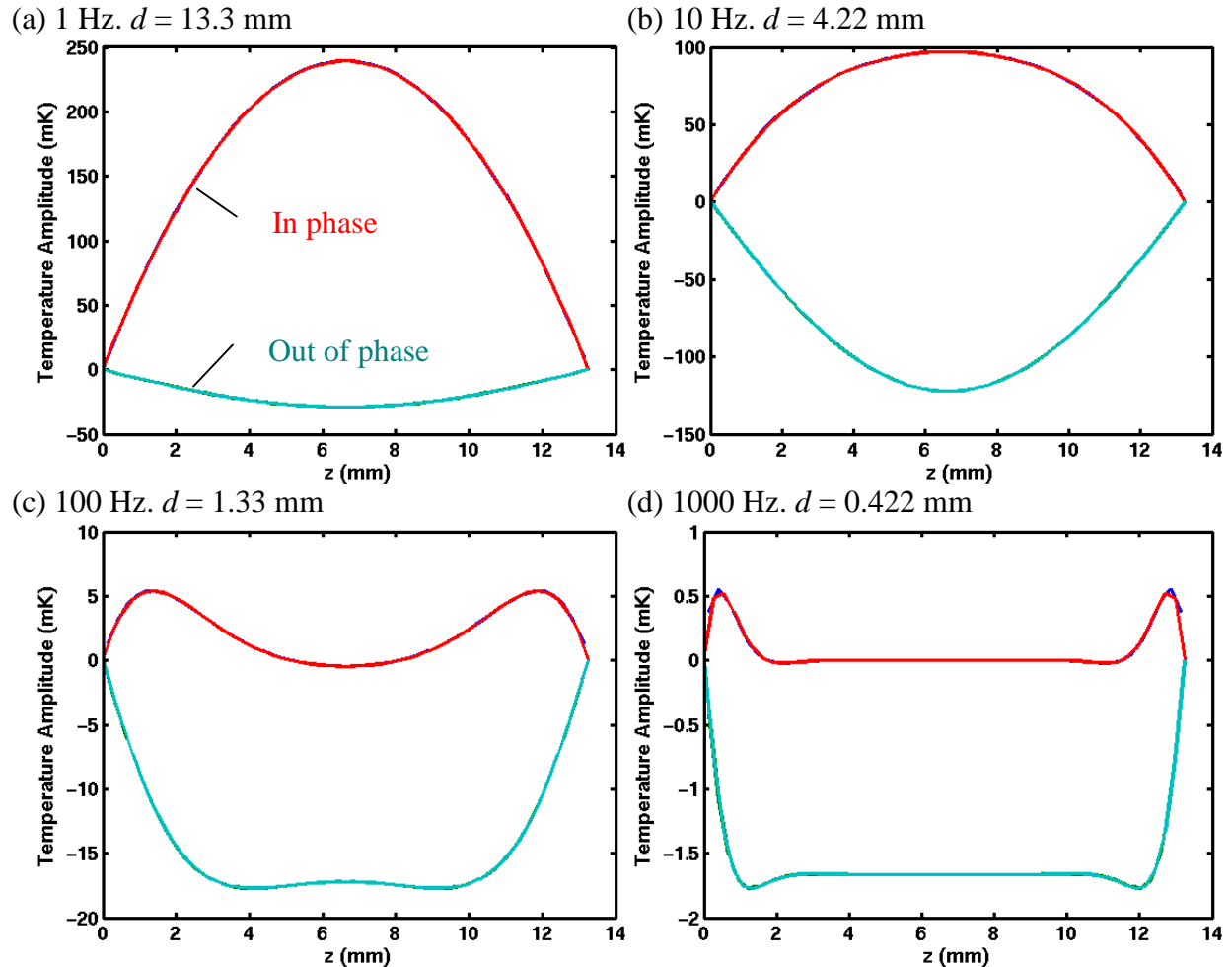


Figure 4.2 Graph of in-phase and out-of-phase temperature amplitudes against distance (z) along the platinum wire at (a) 1 Hz, (b) 10 Hz, (c) 100 Hz, and (d) 1000 Hz. The penetration depths “ d ” are also given.

At 1 Hz, the power is oscillating at a sufficiently low frequency that there is enough time for the temperature to change in phase with the power and the in-phase component dominates.

At the upper frequency range (100 Hz and greater), there is insufficient time for the temperature gradient beginning at the heat baths to extend far into the center of the wire. This is illustrated by the relative peaks in temperature amplitude near the heat baths at higher frequencies (Figures 4.2c and 4.2d). Similar behavior was found in Ref. 8. It is also at these frequencies that the imaginary component dominates the real component, and thus the temperature becomes out of phase with the power as seen in Figure 4.1.

Similar steady-state solutions were obtained over a broad range of frequencies, and the

average temperature amplitude at each frequency was obtained by averaging over the platinum cells between the voltage leads (see Figure 1.1). The results are plotted in Figure 4.3 with the conductivity and specific heat chosen to best match the experimental data.

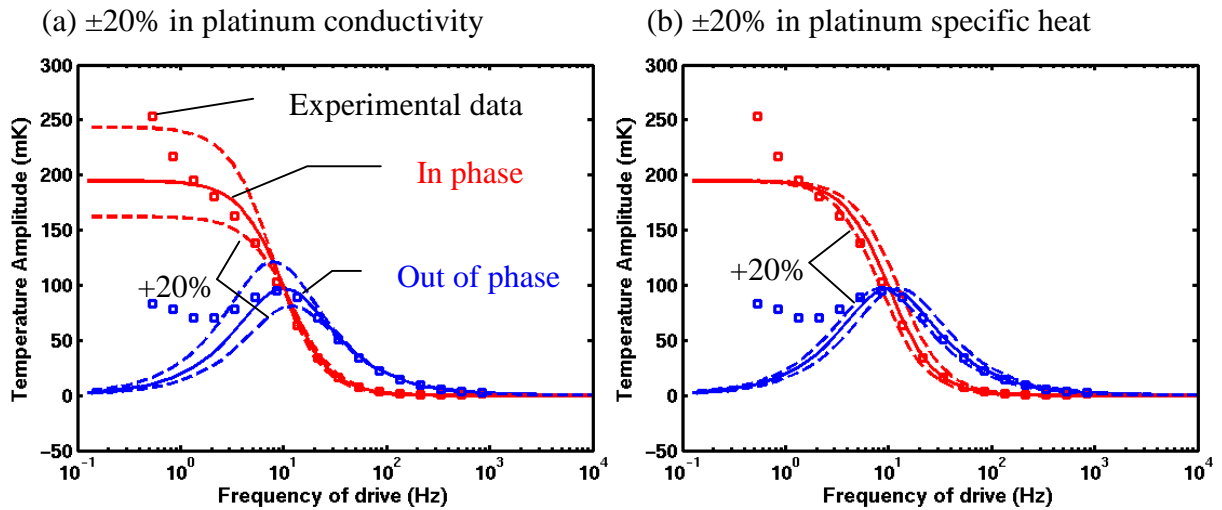


Figure 4.3 The in-phase and out-of-phase temperature amplitudes as a function of frequency. The model predictions are shown by the solid curves. The dashed curves show $\pm 20\%$ variations in (a) the conductivity and (b) the specific heat of the platinum.

In the low frequency limit, the calculated temperature amplitudes are dominated by the in-phase component, while the out-of-phase component falls to zero. In the high frequency limit, the out-of-phase component dominates, and the in-phase component falls to zero. The data is evidently flawed at less than 10 Hz, since the in-phase component should approach a constant and the out-of-phase component should fall to zero. The distinctive shapes of the real and imaginary curves and the close agreement between simulation and experiment above 10 Hz allowed for the simultaneous determination of both thermal conductivity and specific heat. The thermal conductivity and specific heat of the platinum wire, assumed to be $7.5 \mu\text{m}$ in radius, were determined to be $530 \text{ W/m}\cdot\text{K}$ and $2.8 \times 10^5 \text{ J/m}^3\cdot\text{K}$, respectively, with an uncertainty of about $\pm 10\%$ since the curves in Figure 4.3 with $\pm 20\%$ variations provide poorer fits. These values differ from the literature values of $430 \text{ W/m}\cdot\text{K}$ and $1.92 \times 10^5 \text{ J/m}^3\cdot\text{K}$.¹⁴

Changes of $\pm 20\%$ in the platinum conductivity (Figure 4.3a) shift the temperature

amplitude curves both vertically and horizontally. Increasing the conductivity allows heat to be more easily conducted out to the heat baths, shifting the curves down. The results do not depend on conductivity in the high frequency limit. Changes of $\pm 20\%$ in the specific heat (Figure 4.3b) shift the curves horizontally. Increases in the specific heat shift the curves to the left. The high and low frequency limits remain unaffected. The results do not depend on specific heat in the low frequency limit.

There is, however, another uncertainty in these values due to the uncertainty of the wire radius, which was measured by a light microscope as $7.5 \mu\text{m}$. Errors associated with diffraction at the wire's edge are on the order of the wavelength of the light, which is approximately $1 \mu\text{m}$ and significant in comparison to the radius. An identical fit can be obtained using the standard values of thermal conductivity and specific heat if the radius is adjusted from $7.5 \mu\text{m}$ to $8.4 \mu\text{m}$ (a 12% increase). In the rest of this work, the literature values will be used for platinum under the assumption that the wire radius was $8.4 \mu\text{m}$.

4.2 Gaseous Deuterium

The 2D model is essential when deuterium is included, since heat can now flow in the R direction. The 2D effects are illustrated in Figure 4.4, which shows significant nonuniformity along the wire at 10 Hz. The wire can barely be seen, as it is just the inner $8.4 \mu\text{m}$.

The effects on the temperature amplitude due to the side heat baths in the 2D model are qualitatively similar to those found from the 1D model. The temperature amplitudes along Z have the arch shape as in the 10 Hz case of Figure 4.2b. The maximum [in-phase, out-of-phase] temperature amplitudes have been reduced from [100 mK, 130 mK] to [52 mK, 19 mK], because the heat deposited in the platinum wire is conducted into the gas.

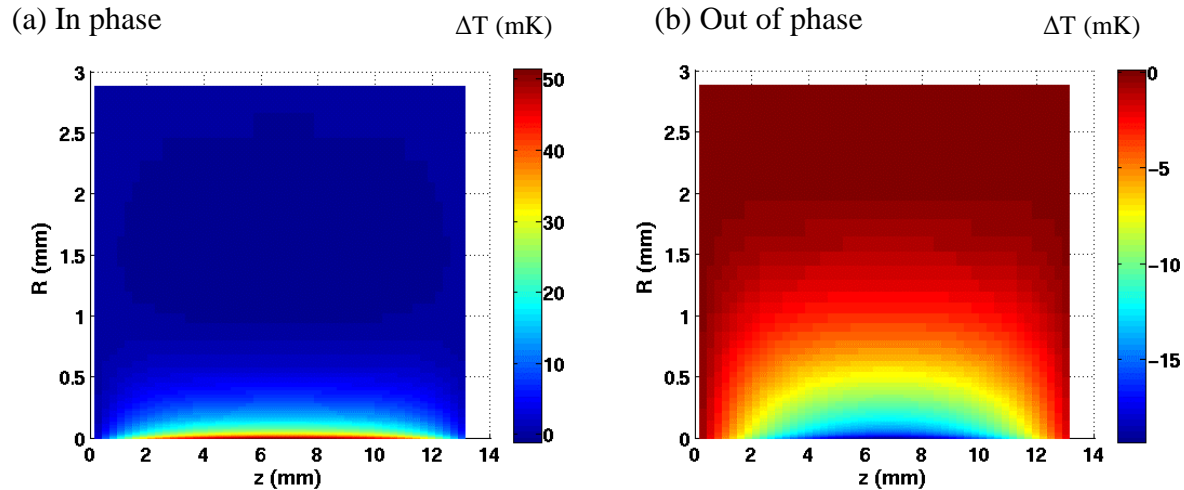


Figure 4.4 Temperature amplitudes for a platinum wire in gaseous deuterium at 10 Hz split into (a) in-phase and (b) out-of-phase components.

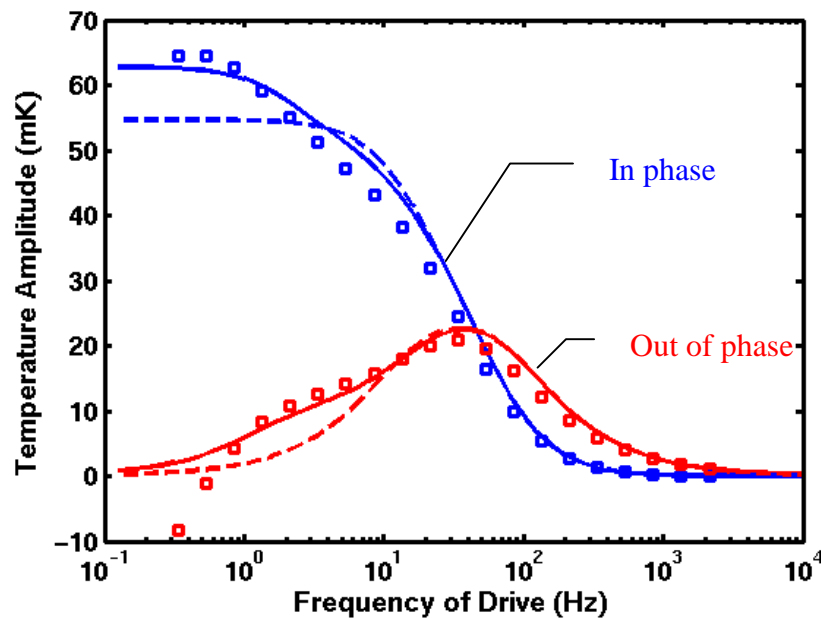


Figure 4.5 In-phase and out-of-phase temperature amplitudes as a function of drive frequency for a platinum wire in 21.0 torr of deuterium gas at 20.9 K. The solid line indicates that the wall heat bath is at 3 mm and the dashed line indicates 1 mm.

From Figure 4.5 (similar to Figure 4.3 but for deuterium gas), the thermal conductivity of deuterium gas was determined to be $0.0137 \text{ W/m}\cdot\text{K}$, which is 37% greater than the value of $0.010 \text{ W/m}\cdot\text{K}$ quoted in Ref. 15. This fit was obtained with a specific heat of $360 \text{ J/m}^3\cdot\text{K}$, which is 7.5% greater than the original of $335 \text{ J/m}^3\cdot\text{K}$.¹⁵ Despite being flawed at the low frequency range below 1 Hz, where the imaginary component goes negative, the data is fit well by the model.

The radial distance of the platinum wire to the wall heat bath in the experiment ranged

from 1 mm to 3 mm. Deuterium gas shows a significantly better fit with the wall heat bath at 3 mm (Figure 4.5). The effects of the wall heat bath can be isolated by examining the 1D solution in R , disallowing heat flow to the side heat baths. Heat is deposited in the platinum, flows across the platinum-deuterium boundary into the deuterium, and finally flows into the wall heat bath.

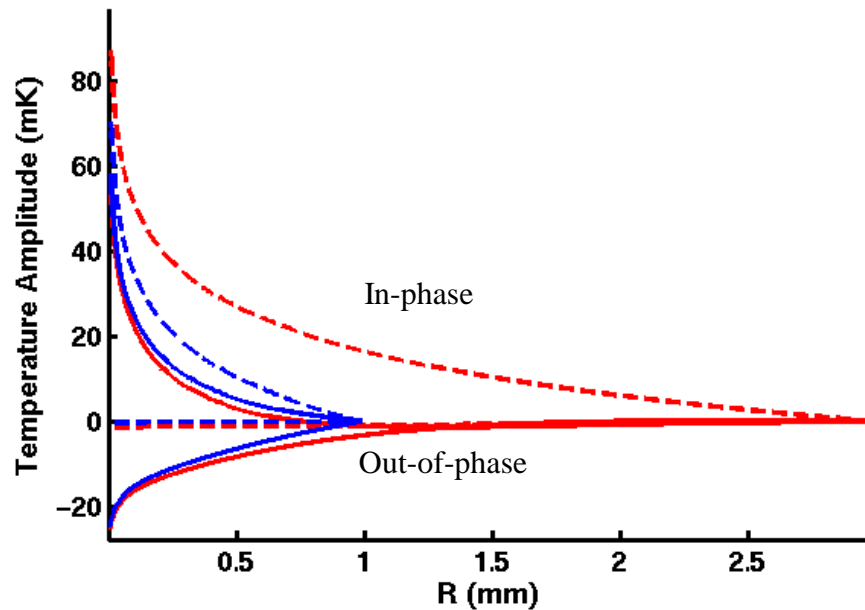


Figure 4.6 Temperature amplitudes against radius R in deuterium gas at 20.9 K. The blue and red indicate the wall heat bath at 1 and 3 mm, respectively. Solid lines show 10 Hz and dashed lines show 0.1 Hz. In-phase amplitudes are positive and out-of-phase amplitudes are negative.

In Figure 4.6, the solid red and blue curves show 10 Hz temperature amplitudes along R with the wall heat bath at 3 mm and 1 mm, respectively. Since the penetration depth is much less than 1 mm, there is only a small difference in the temperature profiles between the two cases. The dashed curves are the same except that the frequency is 0.1 Hz. The large penetration depth at the lower frequency is disrupted by the wall heat bath, causing the maximum in-phase temperature in the 1 mm case [69 mK] to be significantly lower than that of the 3 mm case [84 mK]. The decrease in temperature amplitude that results from decreasing the radial distance of the wall heat bath is also seen in Figure 4.5. Only the parts of the curves less than a certain frequency threshold (~ 10 Hz) are affected, since the smaller penetration depths at frequencies above the threshold do not confront the wall heat bath. Thus the wall heat bath is sufficiently far from the wire to not affect the value of thermal conductivity obtained from Figure 4.5.

4.3 Liquid Deuterium

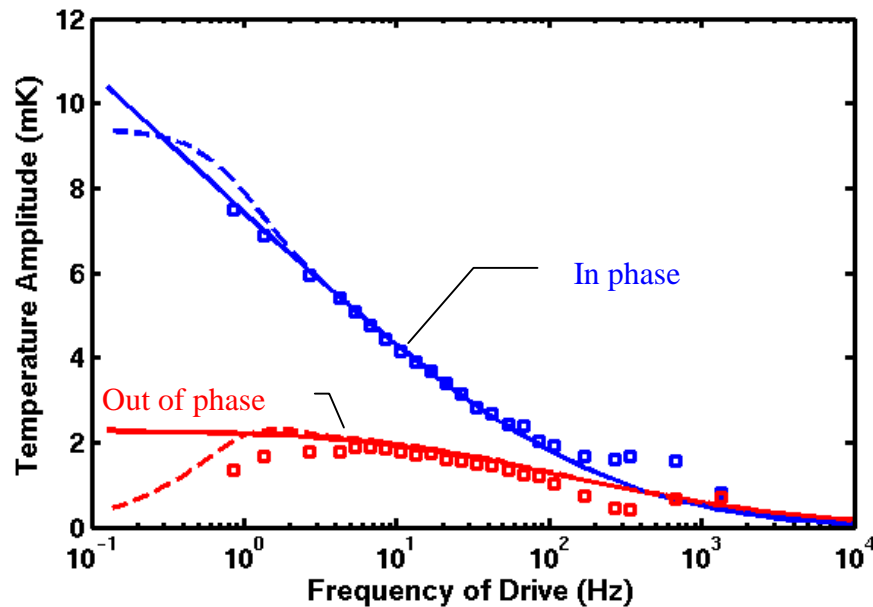


Figure 4.7 In-phase and out-of-phase temperature amplitudes as a function of drive frequency for a platinum wire in liquid deuterium at 24.3 K. The solid lines indicate that the wall heat bath is at 1 mm and the dashed lines indicate 0.2 mm.

A comparison of predictions and experimental data for liquid deuterium is shown in Figure 4.7. The agreement is generally good, but the out-of-phase data is suspect of premature falloff at 10 Hz and less. In an attempt to explain this behavior, the wall heat bath was moved closer in the simulation, to 0.2 mm (dashed curves). However, this fails to provide a convincing fit, and the closest heat bath in the experiment was at 1.0 mm. The distance of the wall heat bath only affects the low frequency range. The structure seen between 100 Hz and 1000 Hz is also questionable and may be due to a thin layer of frozen air between the platinum and the deuterium. The range of good data between 10 Hz and 100 Hz is insufficient to determine both thermal conductivity and specific heat. Yet a good fit was obtained using the standard specific heat, $1.29 \times 10^6 \text{ J/m}^3 \cdot \text{K}$, and the standard thermal conductivity, $0.135 \text{ W/m} \cdot \text{K}$.¹⁵

4.4 Solid Deuterium

From Figure 4.8, the thermal conductivity of solid deuterium was determined to be $0.40 \text{ W/m} \cdot \text{K}$, which is 46% greater than the original $0.274 \text{ W/m} \cdot \text{K}$.¹⁵ This fit was obtained with the standard specific heat of $5.68 \times 10^5 \text{ J/m}^3 \cdot \text{K}$.¹⁵ The data is very good in the limited range, but this

also contributes to uncertainty. Without a distinguishing shape such as seen in Figures 4.3 and 4.5, the conductivity and specific heat cannot both be absolutely determined, as different combinations of conductivity and specific heat can produce the same fit.

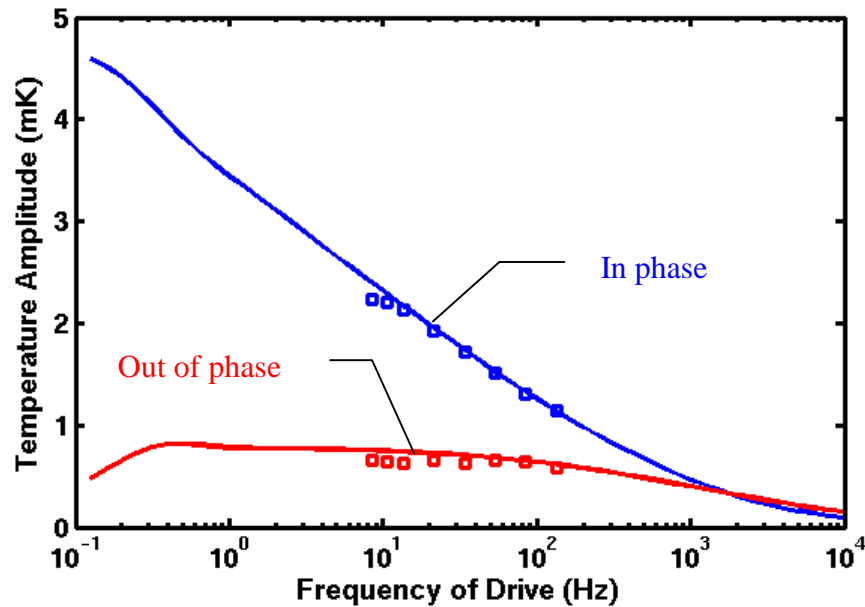


Figure 4.8 In-phase and out-of-phase temperature amplitudes as a function of drive frequency for a platinum wire in deuterium solid at 18.6 K.

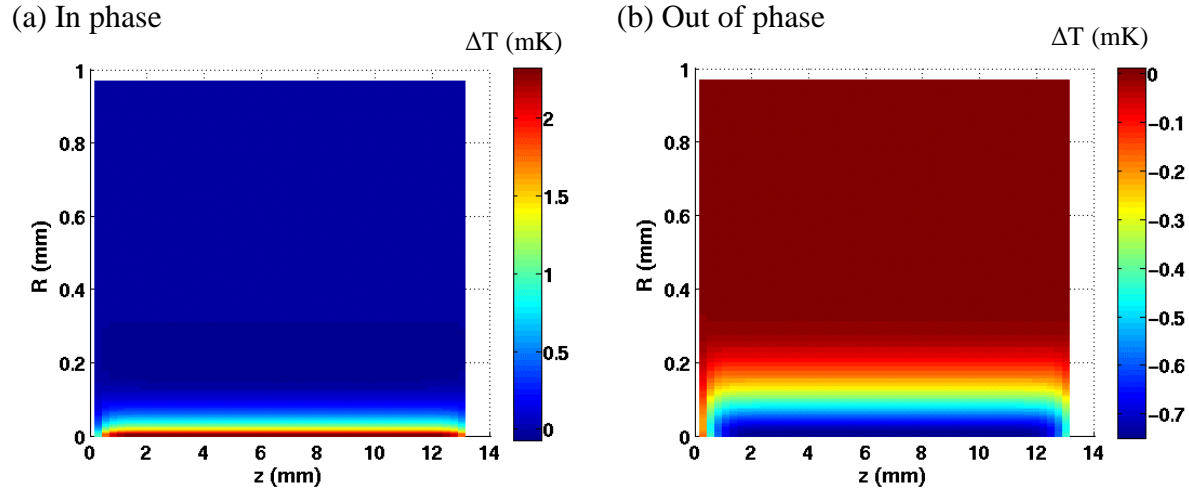


Figure 4.9 Temperature amplitudes of solid deuterium at 10 Hz split into (a) in-phase and (b) out-of-phase components, showing the relative uniformity of temperature amplitudes in Z.

In solid deuterium, temperature amplitudes are more uniform in Z (Figure 4.9) compared with gaseous deuterium (Figure 4.4) because the relatively high specific heat of solid deuterium results in smaller temperature amplitudes; thus the heat flow along Z (proportional to $\partial T / \partial z$) is much smaller.

5. Summary

Improved values of thermal conductivity and specific heat of cryogenic deuterium have been obtained by a new 2D computer program and are summarized in Table 5.1. The program is able to fit data sets for gaseous, liquid, and solid deuterium. The program has confirmed the published values of thermal conductivity and specific heat for platinum. The 2D model provides a more accurate representation than conventional 1D solutions, and has demonstrated that the 3 ω method can be applied to cryogenic deuterium. The adaptation of the Incomplete Cholesky Conjugate Gradient¹³ method to use complex coefficients is believed to be new.

Table 5.1. Determined values of thermal conductivity and specific heat of deuterium, where values in parentheses are previous best values obtained from Ref. 15.

	Thermal Conductivity (W/m·K)	Specific Heat (J/m³·K)
D₂ Gas 20.9 K	0.0137 (0.010)	360 (335)
D₂ Liquid 24.3 K	0.135 (0.135)	1.29×10 ⁶ (1.29×10 ⁶)
D₂ Solid 18.6 K	0.400 (0.274)	5.68×10 ⁵ (5.68×10 ⁵)

Future work should include the acquisition and analysis of improved experimental data. There are some obvious problems with the data: in the case of gaseous deuterium, there is a drop to negative out-of-phase temperature amplitudes below 1 Hz, and in the case of liquid deuterium, there is an unpredicted falloff below 10 Hz and structure between 100 Hz and 1000 Hz. Possible experimental improvements may be to increase the spectral range of the data and improve the measurement of the wire diameter.

In spite of the problems with some of the data, most of the data was found to be of good quality allowing improved values of the thermal conductivity of deuterium to be obtained. These values will be used to model cryogenic target behavior and to improve target quality.

Acknowledgements

I would especially like to thank Dr. Craxton for his time and inspirational guidance throughout this project, and for providing me with the opportunity to work at the Laboratory for Laser Energetics. I would also like to thank Mr. Roger Gram for making this project possible. Finally, I thank everyone in the 2007 High School Summer Program for being an excellent friend.

References

- ¹D. R. Harding *et al.*, Phys. Plasmas **13**, 056316 (2006).
- ²R. W. Powers *et al.*, J. Am. Chem. Soc. **76**, 5974 (1954).
- ³D. G. Cahill and R. O. Pohl, Phys. Rev. B **35**, 4067 (1986).
- ⁴N. O. Birge and S. R. Nagel, Rev. Sci. Instrum. **58**, 1464 (1987).
- ⁵L. Lu, W. Yi, and D. L. Zhang, Rev. Sci. Instrum. **72**, 2996 (2001).
- ⁶A. Jacquot *et al.*, J. Appl. Phys. **91**, 4733 (2002).
- ⁷F. Chen, *et al.*, Rev. Sci. Instrum. **75**, 4578 (2004).
- ⁸C. Dames and G. Chen, Rev. Sci. Instrum. **76**, 124902 (2005).
- ⁹R. Gram, unpublished results (2007).
- ¹⁰D. G. Cahill, Rev. Sci. Instrum. **61**, 802 (1990).
- ¹¹D. G. Cahill, Rev. Sci. Instrum. **73**, 3701 (2002).
- ¹²W. H. Press *et al.*, *Numerical Recipes: The Art of Scientific Computing*, Cambridge University Press, Cambridge, 1986, p. 635.
- ¹³D. S. Kershaw, J. Comput. Phys. **26**, 43-65 (1978).
- ¹⁴V. J. Johnson (ed.), *Properties of Materials at Low Temperature (Phase I) A Compendium*, New York, Pergamon Press, 1961 p4.182.
- ¹⁵P. C. Souers, *Hydrogen Properties for Fusion Energy*, University of California Press, Berkeley, 1986, pp. 67 and 69.

Appendix

This section details the numerical “steady state” solution of (3-1) and the calculation of the quindagonal matrix coefficients of (3-4). Integrating the heat equation (3-1) over the volume of cell i (see Figure A.1) gives

$$C_{mi}\Delta V_i \frac{\partial T_i}{\partial t} + [\Delta S_i^{(N)} Q_i^{(N)} - \Delta S_i^{(S)} Q_i^{(S)} + \Delta S_i^{(E)} Q_i^{(E)} - \Delta S_i^{(W)} Q_i^{(W)}] = W_i \Delta V_i \quad (\text{A-2})$$

where C_{mi} is the specific heat of cell i , ΔS_i are the cell interface areas, and ΔV_i is the cell volume.

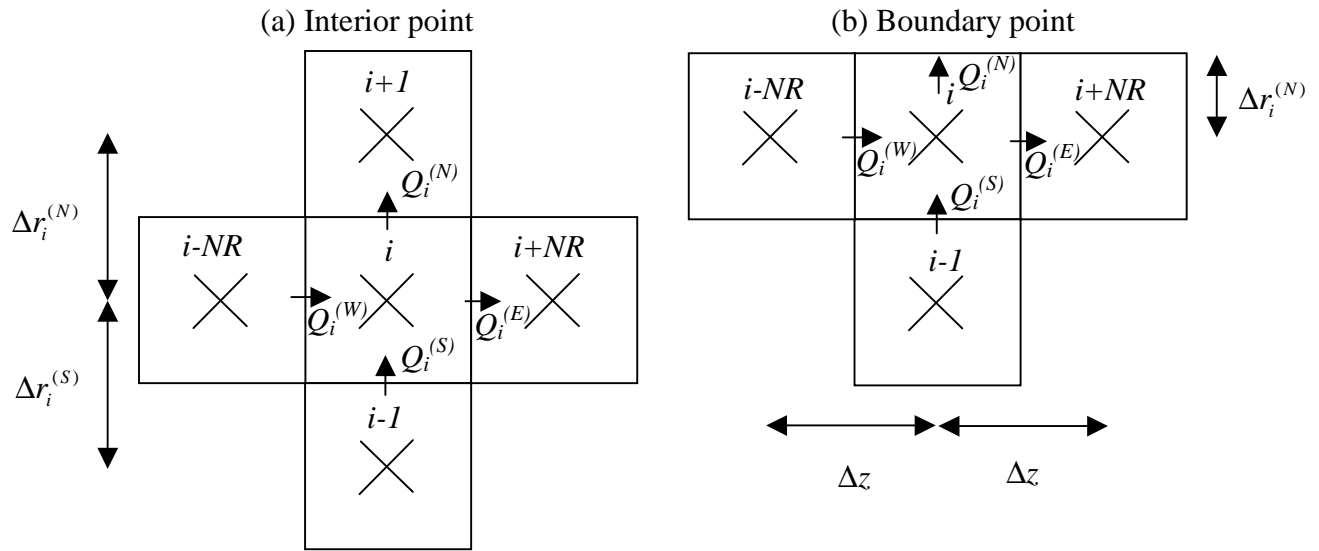


Figure A.1 (a) A typical interior cell with the heat flow Q into its four adjacent cells. (b) A depiction of a point on the wall heat bath. NR is the number of cells in the R direction.

Using $T(r, z, t) = \tilde{T}(r, z)e^{2i\omega t}$ which differentiates to $\frac{\partial T}{\partial t} = 2i\omega\tilde{T}e^{2i\omega t}$ (A-3)

$$Q_i^{(N)} = \frac{-\kappa_i^{(N)}(\tilde{T}_{i+1} - \tilde{T}_i)}{\Delta r_i^{(N)}}, \text{ etc. for interior points} \quad (\text{A-4})$$

$$Q_i^{(N)} = \frac{-\kappa_i^{(N)}(0 - \tilde{T}_i)}{\Delta r_i^{(N)}}, \text{ etc. for boundary points,} \quad (\text{A-5})$$

one finds

$$2i\omega \cdot C_{mi}\Delta V_i - [\delta_i^{(N)}(\tilde{T}_{i+1} - \tilde{T}_i) - \delta_i^{(S)}(\tilde{T}_i - \tilde{T}_{i-1}) + \delta_i^{(E)}(\tilde{T}_{i+NR} - \tilde{T}_i) - \delta_i^{(W)}(\tilde{T}_i - \tilde{T}_{i-NR})] - [\beta_i^{(N)}(\tilde{T}_0 - \tilde{T}_i) - \beta_i^{(S)}(\tilde{T}_i - \tilde{T}_0) + \beta_i^{(E)}(\tilde{T}_0 - \tilde{T}_i) - \beta_i^{(W)}(\tilde{T}_i - \tilde{T}_0)] = W_i \Delta V_i \quad (\text{A-6})$$

where

$$\delta_i^{(N)} = \frac{\Delta S_i^{(N)} \kappa_i^{(N)}}{\Delta r_i^{(N)}}, \quad \delta_i^{(S)} = \frac{\Delta S_i^{(S)} \kappa_i^{(S)}}{\Delta r_i^{(S)}}, \quad \delta_i^{(E)} = \frac{\Delta S_i^{(E)} \kappa_i^{(E)}}{\Delta z}, \quad \delta_i^{(W)} = \frac{\Delta S_i^{(W)} \kappa_i^{(W)}}{\Delta z} \quad (\text{A-7})$$

$$\beta_i^{(N)} = \frac{\Delta S_i^{(N)} \kappa_i^{(N)}}{\Delta r_i^{(N)}}, \quad \beta_i^{(S)} = 0, \quad \beta_i^{(E)} = \frac{\Delta S_i^{(E)} \kappa_i^{(E)}}{\Delta z/2}, \quad \beta_i^{(W)} = \frac{\Delta S_i^{(W)} \kappa_i^{(W)}}{\Delta z/2} \quad (\text{A-8})$$

Here $\Delta S_i^{(N)}$ is the surface area of the interface, $\kappa_i^{(N)}$ is the thermal conductivity, $\tilde{T}_0 = 0$, and Δr_i and Δz are the distances between cell centers in R and Z, respectively.

The terms δ_i represent the heat flow across interfaces between typical (interior) cells while β_i represents the heat flow across boundaries. The terms δ_i and β_i for each interface are exclusively chosen, i.e., one must be zero. There is no heat flow across the lower boundary, since it is the exact center of the symmetric cylinder of the 3D depiction of the model (Figure 2.1b). The fluxes across the east and west side heat baths are represented similarly to the wall heat bath, except that $\Delta z/2$ is the distance in Z from the cell center to the side heat bath.

Equation (A-6) can be expressed as

$$E_i \tilde{T}_{i-NR} + A_i \tilde{T}_{i-1} + B_i \tilde{T}_i + C_i \tilde{T}_{i+1} + F_i \tilde{T}_{i+NR} = D_i, \quad (\text{A-9})$$

$$\text{where } E_i = -\delta_i^{(W)} \quad (\text{A-9.1})$$

$$A_i = -\delta_i^{(S)} \quad (\text{A-9.2})$$

$$B_i = 2i\omega \cdot C_{mi} \Delta V_i + \delta_i^{(N)} + \delta_i^{(S)} + \delta_i^{(E)} + \delta_i^{(W)} + \beta_i^{(N)} + \beta_i^{(S)} + \beta_i^{(E)} + \beta_i^{(W)} \quad (\text{A-9.3})$$

$$C_i = -\delta_i^{(N)} \quad (\text{A-9.4})$$

$$F_i = -\delta_i^{(E)} \quad (\text{A-9.5})$$

$$D_i = W_i \Delta V_i \quad (\text{A-9.6})$$

The system of simultaneous equations forms a quindagonal matrix equation (3-4) that

can be solved by Kershaw's iterative ICCG¹³ method, adapted to provide complex solutions for \tilde{T}_i . In 1D cases, a pair of diagonals becomes zero, and the matrix equation simplifies to a tridiagonal matrix that can be solved easily. With minor modifications to (A-9.1) to (A-9.6), the initial value equation (3-3) can also be solved.